

pubs.acs.org/JACS Article

Directly Oxidizing Ethanol to Glycolic Acid over a Single-Rh-Site Catalyst via Water-Mediated Oxygen Shuttle

Bin Li, → Jiali Mu, → Guifa Long, → Xiangen Song,* Yang Zhao, Ende Huang, Siyue Liu, Yao Wei, Fanfei Sun, Siquan Feng, Qiao Yuan, Xingju Li, Yutong Cai, Yue Zhang, Wenrui Dong, Weiqing Zhang, Xueming Yang, Dehui Deng, Li Yan,* and Yunjie Ding*



Cite This: J. Am. Chem. Soc. 2025, 147, 29052-29064



ACCESS

Metrics & More

Article Recommendations

Supporting Information

ABSTRACT: Direct oxidation of ethanol to glycolic acid in aqueous solutions under mild conditions offers opportunities for sustainable chemistry. Herein, we report a water-mediated oxygen-shuttle mechanism on S/N/I atoms synergistically coordinated single-Rh-site catalysts (Rh₁/AC-SNI₄₀₀) to enable the direct production of glycolic acid from ethanol oxidation with 93% selectivity in liquid products and a TOF of 250 h⁻¹ at 160 °C. Comprehensive characterizations including isotope labeling experiments and theoretical calculations reveal that hydroxyl radicals (\bullet OH), generated via O₂/I-triggered H₂O dissociation, insert into C–I bonds to form hydroxyl groups and meanwhile, replace the original OH in ethanol to form C=O, ensuring that all oxygen atoms of glycolic acid directly originate from H₂O. O₂ enters the system through the decomposition and regeneration of HIO intermediates, completing the oxygen-shuttle cycle driven by sustainable regeneration of water. Furthermore, the optimized S/N/I atoms' synergistical coordination enhances electron delocalization around single-Rh sites, substantially reducing the activation barriers of critical reaction steps and outperforming Rh nanoparticles by 16-fold in activity.



1. INTRODUCTION

Global demands for sustainable energy have intensified efforts toward biomass valorization. Ethanol, as an accessible biomass-derived platform molecule, holds promise for conversion to value-added chemicals. ^{2–5} Beyond conventional applications such as acetaldehyde, ethylene, ethyl acetate, and butanol, 6-9 its transformation to glycolic acid (GA) remains underexplored. GA is an important raw material used in the production of biodegradable materials. Current GA synthesis routes face critical limitations. Although conventional glycolonitrile hydrolysis and formaldehyde carbonylation achieve high yields (99.18%) and selectivity (99.15%) under 100-120 °C, the former uses cyanide in the production process, and the latter has a reaction pressure of more than 8 MPa, which places stringent requirements on the equipment. 10-14 Chloroacetic acid hydrolysis can reach yields of up to 88.17%, the process incurs high production costs and requires prolonged processing times. 15 In addition, the processes of preparing glycolic acid from oxalic acid electrolysis and from hydrogenation of dimethyl oxalate are also under development. 16 The former approach delivers merely 38.7% glycolic acid selectivity while exhibiting relatively high energy intensity. The latter approach typically employs Cu-based catalysts, which are prone to sintering and subsequent deactivation.¹⁷ Bitter et al. reported that copper and nickel nanoparticles supported on carbon nanofibers could oxidize ethylene glycol to glycolic acid under alkaline conditions. 18 Although it achieves a TOF of 39

h⁻¹ with 96% glycolic acid selectivity at 180 °C. The mandatory alkaline reaction environment will cause the risk of catalyst deactivation and increase the cost of product separation. The direct oxidation of ethanol to glycolic acid has not been reported before. Therefore, developing a new route to convert ethanol to glycolic acid with high catalytic performance is attractive, while there remain significant challenges. The emergence of single-atom catalysts has brought breakthrough opportunities for the above path.

Heterogeneous single-metal-site catalysts (HSMSCs) have emerged as a significant class of highly efficient catalysts in recent years, characterized by nearly 100% atomic utilization and unique catalytic properties. These catalysts effectively bridge the gap between heterogeneous and homogeneous catalysis, offering a platform for understanding the nature of active sites at the molecular level. Hutchings et al. achieved hydrogen production from bioethanol reforming by constructing a Ni/MTAC catalyst with a hybrid structure of single atoms and nanoclusters. They revealed a synergistic mechanism in which Ni single atoms promote electron transfer and

Received: May 4, 2025 Revised: July 19, 2025 Accepted: July 21, 2025 Published: July 29, 2025





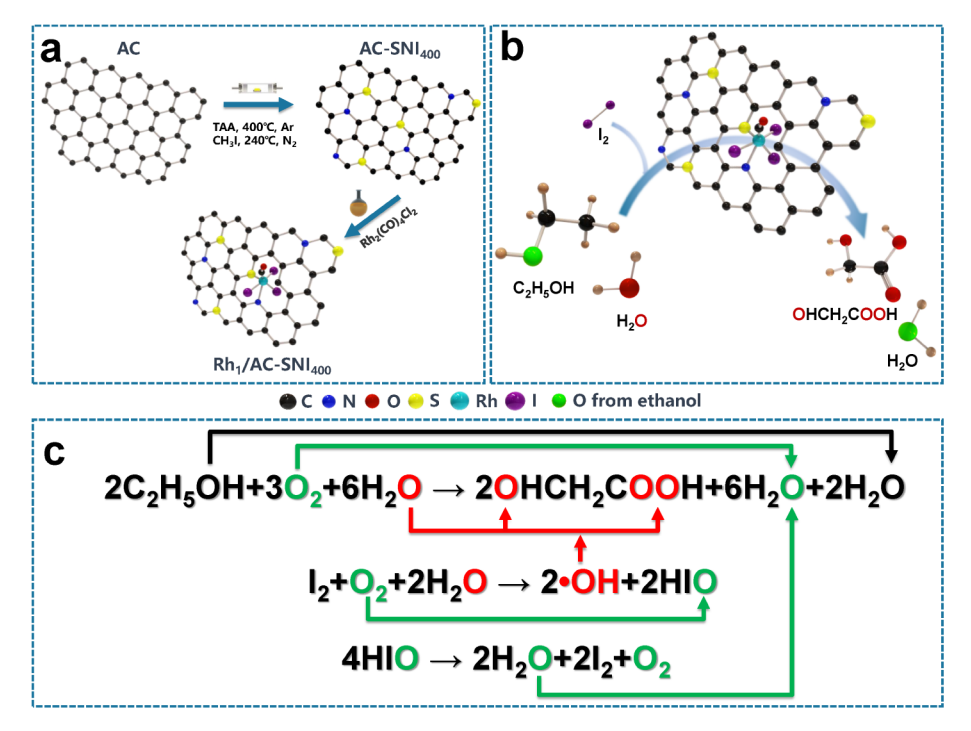


Figure 1. Synthesis of samples. (a) Schematic illustration of the preparation of Rh_1/AC - SNI_{400} catalysts. (b) Schematic diagram of the catalytic process for the direct production of glycolic acid from ethanol. (c) Chemical formula of the catalytic mechanism for water-mediated oxygen shuttling.

enhance intermediate adsorption, while nanoclusters reduce the dehydrogenation energy barrier.²⁴ Li et al. achieved the conversion of ethanol to butene by preparing a new type of dual-single-atom catalyst, Cu₁-Zr₁@SiO₂. The rational design of the double-atom site greatly improved butene selectivity. Activated carbon (AC), known for its low cost, hierarchical pore structure, and excellent thermal and chemical stability, has been widely utilized as a support in heterogeneous catalysis.²⁶ However, its relatively inert surface properties lead to weak interactions between the support and the metal, posing challenges in the precise regulation of the active metal species. 27,28 Recently, various solutions have been proposed to address these issues, with M-N-C materials (where M represents the active metal) gaining significant attention.²⁹ Li et al. developed a nitrogen-doped carbon-supported singlemetal-atom catalyst that has much higher activity in formic acid oxidation than nanoparticles.³⁰ The strong covalent bonds between M and N species effectively regulate the location of the active metal.³¹ Additionally, our previous studies have demonstrated that sulfur species, as ideal electron-donating ligands, can coordinate with the active metal species, further modulating the electron cloud distribution of the active metal and enhancing catalytic activity.³² Iodine species play an essential role in achieving atomic-level dispersion of Rh species on AC support. 33,34 Additionally, molecular iodine is a highly efficient catalyst capable of aerobically iodinating a variety of substrates, such as the hydrogen of β -C in ethanol under mild conditions in the presence of O_2 .

Leveraging insights into multiligand induction, we developed a controllable synthesis of single-site catalysts. Specifically, we engineered S/N/I atom-coordinated Rh single-atom catalysts on activated carbon (Rh₁/AC-SNI₄₀₀) by tuning support pretreatment (Figure 1a). Under the stimulation of I₂ and O₂ at 160 °C, these catalysts directly oxidize ethanol to glycolic acid with 93% selectivity in liquid products and a ca. 250 h⁻¹

turnover frequency (TOF). S/N/I atom coordination enhances electron delocalization around Rh, lowering energy barriers for substrate adsorption and the rate-limiting step (Figure 1b). Activated iodine radicals abstract ethanol's β -C—H, diverting the pathway from acetaldehyde formation. We also revealed a novel water-mediated oxygen-shuttle mechanism: •I and •OH radicals successively abstract and insert into ethanol's C—H bonds. The highly reactive •OH radicals will also replace the original OH of ethanol to form C=O, ensuring that all glycolic acid oxygen atoms are derived from water (Figure 1c). O₂ reacts with •I and H-species to form HIO, which decomposes to regenerate H₂O and O₂, completing the catalytic cycle. This study provides new insight into the role of water in catalytic reactions.

2. RESULTS AND DISCUSSION

2.1. Catalyst Characterization. The Rh₁/AC-SNI₄₀₀ catalyst was synthesized through strong interactions between Rh and the modified activated carbon (AC) containing N, S, and I ligands (details in the Experimental Procedures). AC was first codoped with S and N through thermal treatment with thioacetamide at 400 °C, followed by the introduction of I. Then, the modified AC-SNI₄₀₀ was coordinated with Rh at ambient temperature, resulting in the preparation of the Rh₁/ AC-SNI₄₀₀ catalyst (Figures 1a and S8). For comparison, the AC support with different pretreatment temperatures and their corresponding catalysts were prepared using a similar procedure, denoted as Rh/AC-SNI₆₀₀ and Rh/AC-SNI₈₀₀. We first explored the microstructural properties of Rh₁/AC-SNI₄₀₀ and comparative catalysts through nitrogen adsorption-desorption, thermogravimetric analysis, scanning electron microscopy (SEM), and Raman spectroscopy experiments (Figures S1-S4 and Table S1). These preliminary characterizations display the features of the support and corresponding catalysts, such as high specific surface areas, hierarchical porous

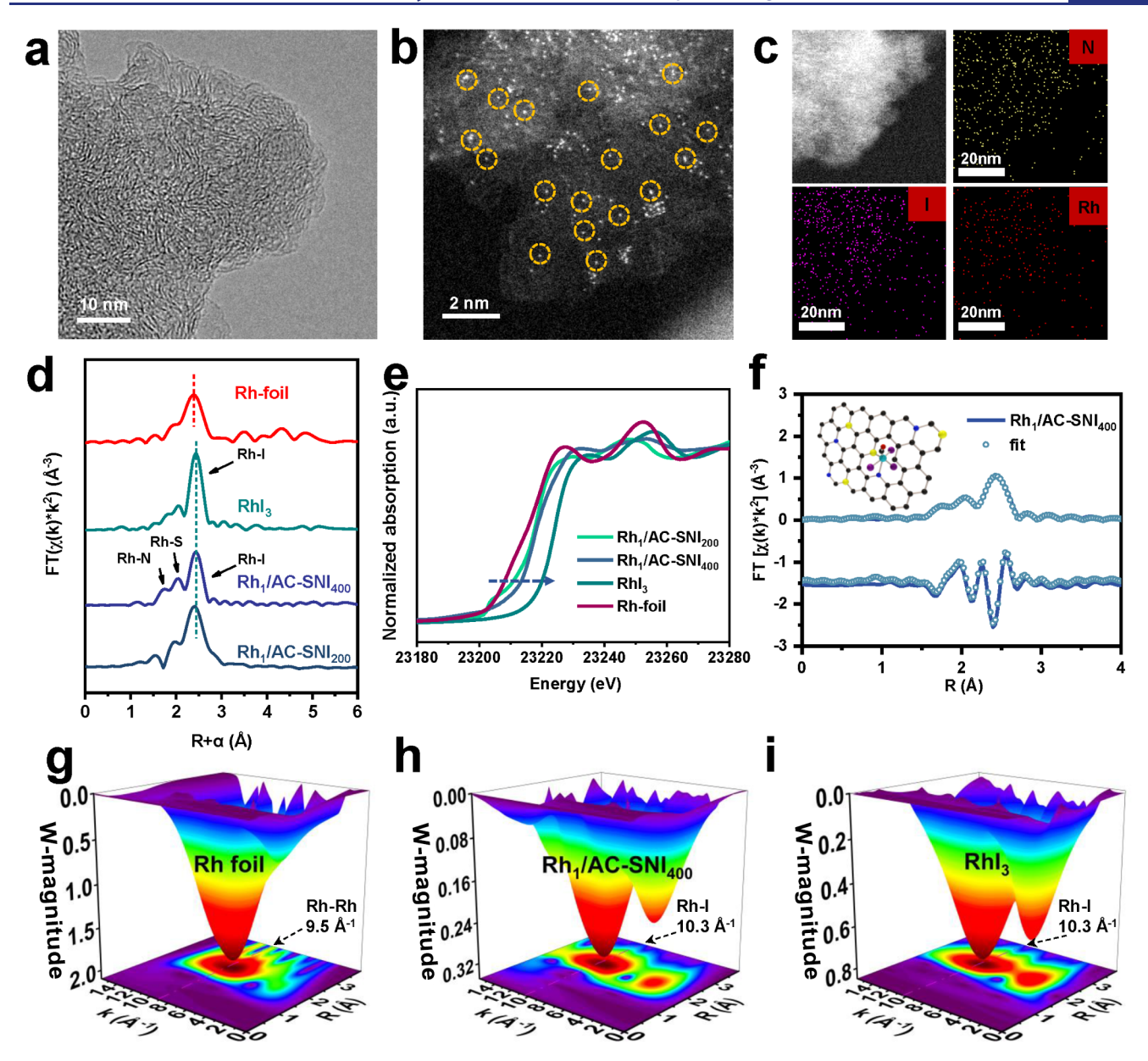


Figure 2. Structural characterization of samples. (a) HR-TEM images of fresh Rh_1/AC - SNI_{400} . (b) HAADF-STEM image of fresh Rh_1/AC - SNI_{400} . (c) HAADF-EDS mapping of fresh Rh_1/AC - SNI_{400} . (d) The experimental curve of k^2 -weighted EXAFS spectra in R-space of Rh foil, RhI₃ and Rh₁/AC- SNI_{400} . (e) XANES spectra for Rh foil, RhI₃ and Rh_1/AC - SNI_{400} . (f) The fitted EXAFS spectra of Rh_1/AC - SNI_{400} and the fitting model (FT magnitude and imaginary component). The wavelet transform contour plots of k^2 -weighted $\chi(k)$ EXAFS signals of (g) Rh foil, (h) Rh_1/AC - SNI_{400} , and (i) RhI_3 .

distribution, excellent thermal stability, irregularly amorphous morphology, and abundant defect sites on the carbon carrier. Consistent with the XRD spectra (Figures S5 and S6), the high-resolution transmission electron microscopy (HR-TEM) analysis (Figure S8) did not reveal the presence of Rh clusters or nanoparticles (NPs) on Rh₁/AC-SNI₄₀₀. The absence of Rh NPs or clusters was further confirmed in the aberration-corrected high-angle annular dark-field scanning transmission electron microscopy (AC HAADF-STEM) images, showing the atomic dispersion of Rh atoms on Rh₁/AC-SNI₄₀₀ (Figure 2a and b). Energy-dispersive spectroscopy (EDS) mapping verified the uniform distribution of S, N, I, and Rh on the Rh₁/AC-SNI₄₀₀ catalyst (Figure 2c). Nevertheless, XRD and HR-TEM results revealed Rh aggregation with different degrees on Rh/AC-SNI₆₀₀ and Rh/AC-SNI₈₀₀ (Figures S5–S8). This

observation was further corroborated by AC HAADF-STEM (Figure S9), which confirmed the presence of both isolated Rh atoms and Rh NPs of varying sizes on Rh/AC-SNI $_{600}$ and Rh/AC-SNI $_{800}$.

X-ray fine structure spectroscopy was employed to further verify the dispersion and precise coordination environment of Rh species in the Rh₁/AC-SNI₄₀₀ series of catalysts. As shown in Figure 2d and Table S2, the extended X-ray absorption fine structure (EXAFS) of Rh₁/AC-SNI₄₀₀ exhibits a prominent peak at approximately 2.44 Å, which can be attributed to Rh–I coordination. This peak is higher than that of Rh–Rh coordination observed at 2.38 Å in the Rh foil sample. Additionally, a smaller peak at 1.7 Å corresponds to Rh–N coordination, while another peak at 1.4 Å is attributed to Rh–CO coordination. The Rh–S bond distance is determined to

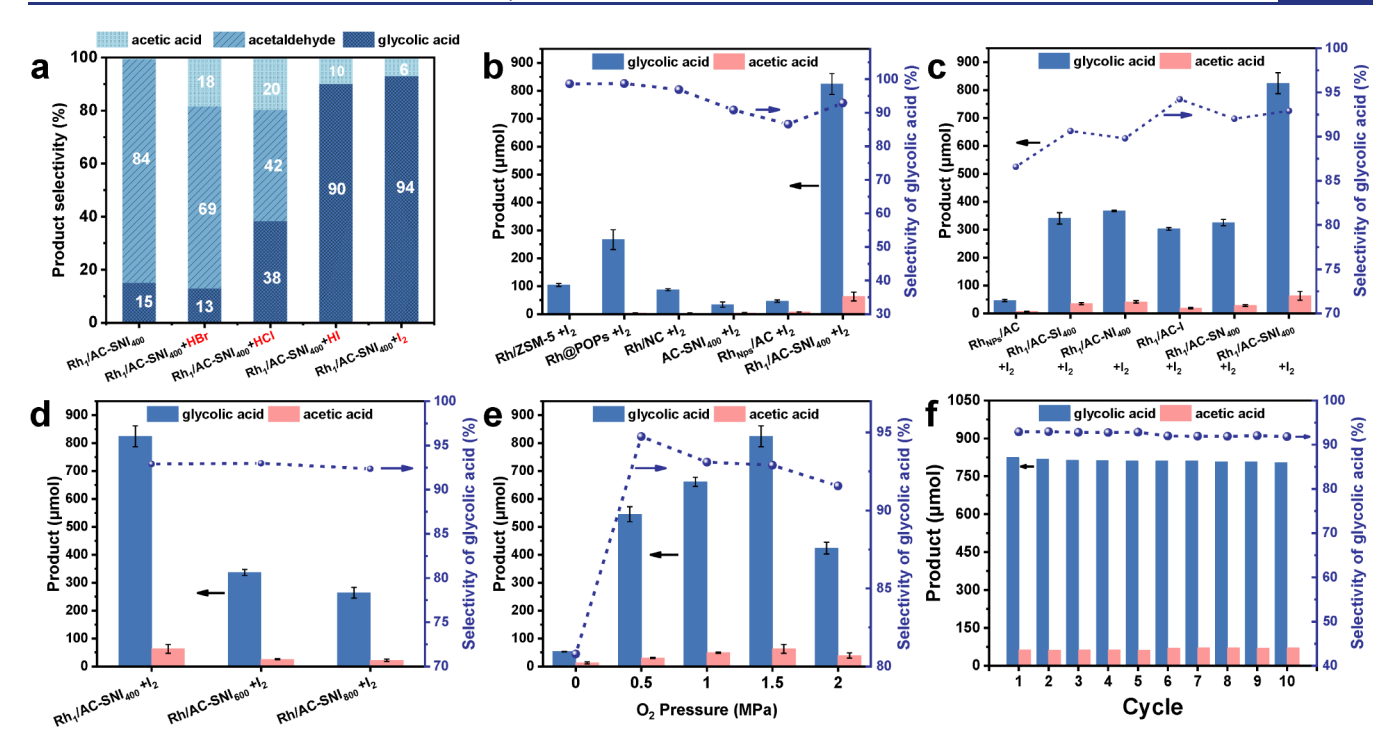


Figure 3. Ethanol oxidation performance and structure—activity relationship. Catalytic activity of (a) different halogen additives on Rh₁/AC-SNI₄₀₀, (b-d) different catalysts, (e) different pressures of O₂ on Rh₁/AC-SNI₄₀₀. (f) Recyclability tests of Rh₁/AC-SNI₄₀₀ (general reaction conditions: T = 150 °C, $P_{\text{oxygen}} = 1.5$ MPa for 1 h, $m_{\text{water}} = 10$ g, $m_{\text{catalyst}} = 50$ mg, $m_{\text{ethanol}} = 0.25$ g).

be 2.0 Å. Detailed EXAFS fitting results (Table S2 and Figure \$10) reveal coordination numbers of 2.66, 1.5, and 1.0 for Rh-I, Rh-N/C, and Rh-S, respectively, indicating that Rh is simultaneously coordinated with I, N, and S, respectively. Xray absorption near-edge structure (XANES) spectra indicate that the Rh absorption edge in Rh₁/AC-SNI₄₀₀ lies between that of the Rh foil and RhI3, suggesting a Rh^{δ^+} species with a valence state between 0 and +3 (Figure 2e). EXAFS wavelet transform analysis was conducted to further examine the coordination environment of Rh species (Figure 2g-i and Figure S11). Two strong peaks were detected at about 4.7 Å⁻¹ and 10.3 Å⁻¹ on Rh₁/AC-SNI₄₀₀, distinct from the only peak of Rh-Rh at 9.5 Å^{-1} , further confirming the atomic dispersion of Rh on Rh₁/AC-SNI₄₀₀. Based on the above characterization results, it is proposed that the Rh₁/AC-SNI₄₀₀ catalyst exhibits single-Rh-site dispersion, existing in a coordination structure of Rh(CO)SNI₃. Moreover, we identified the coordination environments and statuses of Rh₁/AC-NI₄₀₀ and Rh₁/AC-SI₄₀₀ in our previous work, which were determined to be RhN(O=C)(CO) I_3 and RhS(O=C)(CO) $_2I_2$, respectively, in which O=C was the carbonyl oxygen functional group on AC.38

X-ray photoelectron spectroscopy (XPS) was used to further explore the valence state of Rh on the catalysts. As shown in Figure S12 and Table S3, the Rh species on $\mathrm{Rh_1/AC\text{-}SNI_{400}}$ are mainly composed of $\mathrm{Rh^{1+}}$ and $\mathrm{Rh^{3+}}$. However, $\mathrm{Rh^0}$ species appeared on $\mathrm{Rh/AC\text{-}SNI_{600}}$ and $\mathrm{Rh/AC\text{-}SNI_{800}}$, with a higher proportion in $\mathrm{Rh/AC\text{-}SNI_{800}}$. Furthermore, the XPS spectra of S 2p show that the peaks at 163.73 and 164.83 eV can be attributed to the S $\mathrm{2p_{3/2}}$ and $\mathrm{2p_{1/2}}$ signals of thiophene C–S–C species bound to the surface of AC-SNI. The position of S 2p in AC-SNI₄₀₀ shifted to a low energy of about 1 eV compared to that of $\mathrm{Rh_1/AC\text{-}SNI_{400}}$, indicating the coordination between Rh species and S species, and electron transfer

from Rh to S (Figure S13 and Table S4). The peak at 168.8 eV can be attributed to sulfate or sulfite $C-SO_x$ species.^{39–41} The thiophene C-S-C species decrease with the increase of the pretreatment temperature, indicating that the higher pretreatment temperature leads to the oxidation of thiophene C-S-C to sulfate or sulfite. Furthermore, multiple nitrogen species were found on Rh₁/AC-SNI₄₀₀, which can be attributed to pyridinic N (397.96 eV), metallic N (399.02 eV), pyrrolic-N (400.02 eV), quaternary ammonium nitrogen (400.94 eV), and nitrogen oxide substances (403.31 eV), 42-45 among which metallic-N is the nitrogen species directly coordinated with the single-Rh sites (Figure S14 and Table S5).³⁸ This indicates that the electron cloud around Rh shifts toward the S and N ligands. Due to the stronger electronegativity of the S and N ligands, this movement of the electron cloud results in a shorter bond length for Rh-S and Rh-N, which is more favorable for the attack of ethanol. On the other hand, the XPS results showed that the N and S content on the catalyst gradually decreased with the increase of the pretreatment temperature (Table S6). The results demonstrate that excessively high pretreatment temperatures would lead to the loss of active S and N species on the AC, thereby weakening the ability of the carrier to anchor the single Rh site and causing partial metal aggregation. 46,47

Moreover, we can observe that elements such as Rh and S/N/I are also distributed in the bulk phase of the catalyst by analyzing the time-of-flight secondary ion mass spectrometry (TOF-SIMS) characterization results (Figure S15). This indicates that the S/N/I atom moieties infiltrate the carbon matrix rather than being merely surface-deposited, providing more Rh anchoring sites. Further, Rh₁/AC-SNI₄₀₀ was purged under Ar at 150 °C for 1 h (denoted Rh₁/AC-SNI₄₀₀-purged). Time-of-flight secondary ion mass spectrometry (TOF-SIMS) analysis (Figure S16) revealed only a minimal I-content

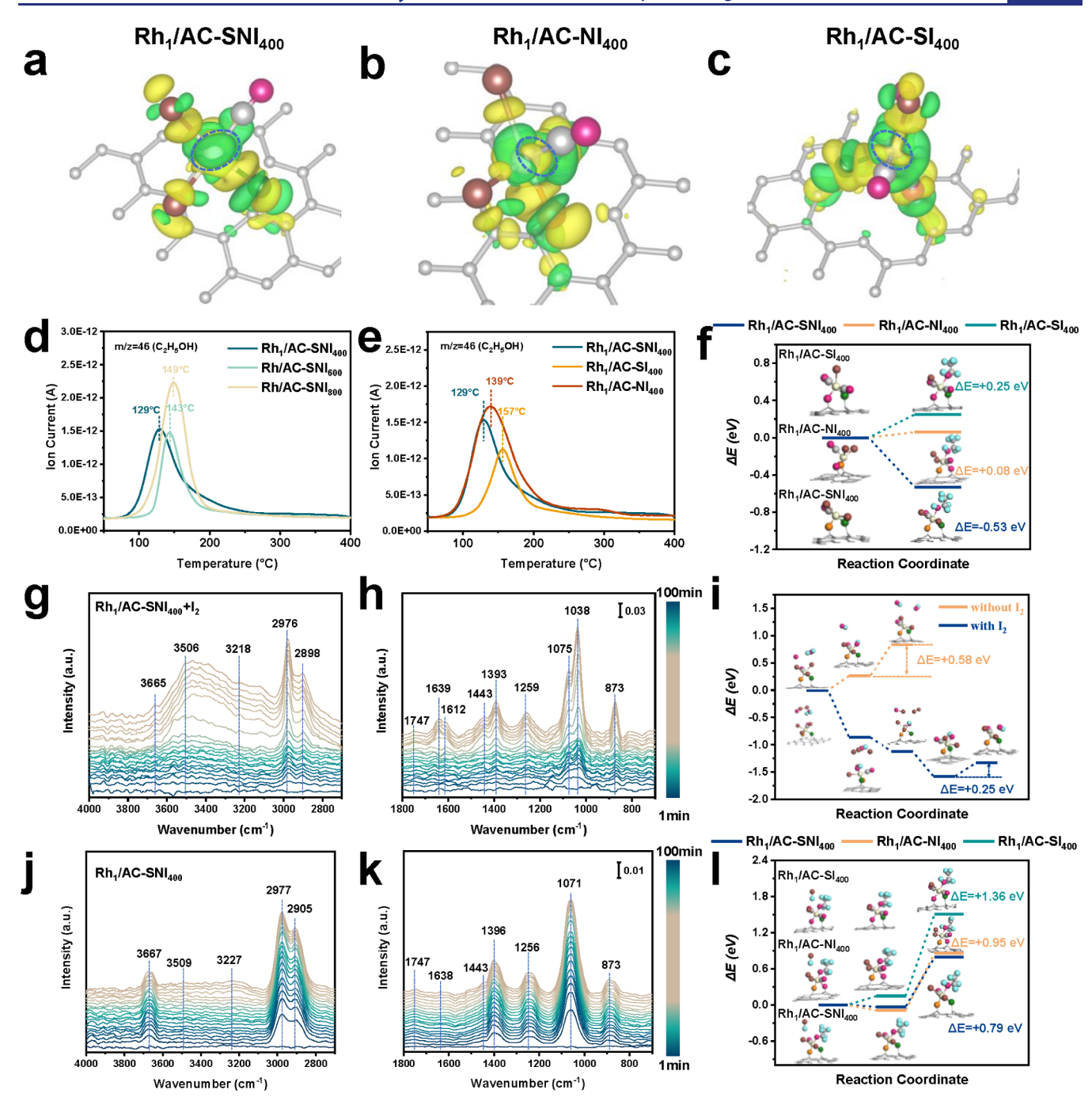


Figure 4. DFT studies and mechanism characterizations of Rh_1/AC catalysts under different coordination environments. (a–c) Optimized structures and charge distribution maps of catalysts with different coordination environments. (Green and yellow colors represent electron depletion and accumulation, respectively.) Temperature-programmed desorption of ethanol (C_2H_5OH -TPD) of (d) catalysts with different pretreatment temperatures. (e) Catalysts with different coordination environments. (f) DFT calculation of the energy barrier for ethanol adsorption on catalysts with different coordination environments. (g,h) In situ DRIFTS spectrum of Rh_1/AC -SNI₄₀₀ with I₂. (i) DFT calculation of the energy barrier for generation of OH from H₂O with and without I₂ activation over Rh_1/AC -SNI₄₀₀. (j,k) In situ DRIFTS spectrum of Rh_1/AC -SNI₄₀₀ with different coordination environments.

decrease in the post-treated sample versus pristine $\mathrm{Rh_1/AC}$ - $\mathrm{SNI_{400}}$, confirming that iodine predominantly chemisorbs onto the carbon framework with a very small proportion of physisorption.

2.2. Catalyst Evaluation. Typically, the reactivity of a series of catalysts was measured by adding 50 mg of catalysts to 10 g of deionized water at 150 $^{\circ}$ C under the conditions of 15 bar O_2 for 1 h. To investigate the role of halogen additives, a series of control experiments with Rh₁/AC-SNI₄₀₀ catalyst was

conducted (Figure 3a and Figure S17). In the absence of halogens, the selectivity in liquid products for glycolic acid was less than 15%. Additionally, in experiments using HBr, it was only 13%. Changing to HCl increased the selectivity in liquid products up to 38%. However, it exceeded 90% with the assistance of HI, and the TOF reached 361.5 h^{-1} (Figure 3a and Figure S18). Due to the corrosiveness of these protonic acids, we chose I_2 as a milder additive. Using I_2 as an additive resulted in a further increase in the selectivity for glycolic acid

in liquid products to 93%, with a little decrease in TOF to 228.2 h⁻¹ at 150 °C. These results demonstrate the essential role of I₂ in the oxidation of ethanol to glycolic acid. Through carrier screening among ZSM-5, porous organic polymer, and nitrogen-doped carbon, it was found that the Rh₁/AC-SNI₄₀₀ catalyst exhibited the highest reactivity. Whereas, the Rh_{NPs}/ AC catalyst with only NPs on AC showed the lowest activity (Figure S8d-f and Figure 3b). This indicates that the single-Rh sites serve as the active sites for this reaction. Furthermore, among the various active metals tested, such as Ir, Ru, Mo, and Pd, the Rh metal exhibited the best performance, three times higher than the second one (Figure S19). Additionally, a series of catalytic activity comparisons with different coordination elements was conducted. As shown in Figure 3c, under the same reaction conditions of I₂ addition, the activities of Rh₁/ AC-SI₄₀₀, Rh₁/AC-NI₄₀₀, Rh₁/AC-I, and Rh₁/AC-SN₄₀₀ were all lower than that of Rh₁/AC-SNI₄₀₀. This indicates that the comprehensive effect of I, N, and S on the catalyst plays a crucial role in regulating the coordination state of Rh, ensuring that the active sites maintain an optimal coordination environment. Figure 3d shows the reaction results of Rh/ AC-SNI₄₀₀₋₈₀₀ catalysts, with a significant decline in activity after support treatment at 600 and 800 °C, further demonstrating that the aggregation of Rh led to the decrease of catalytic activity. The TOF comparisons of all catalysts and actual metal loadings are listed in Tables S7 and S8.

The temperature variation curve results show that the reaction activity is basically zero at 120 °C. With the temperature increasing from 120 to 160 °C, the reaction activity significantly increases to a TOF of 251 h⁻¹, and the selectivity of glycolic acid in liquid products also gradually increases to 93% (Figure S20), indicating that overcoming the energy barrier of the rate-determining step for generating glycolic acid requires a starting activation temperature. As the reaction temperature increased from 120 to 160 °C, ethanol conversion rose from 3% to 28%, while CO₂ selectivity decreased from 71% to 24.8%. Under these conditions, the primary byproducts were CO₂ and acetic acid. As the reaction time prolongs, it can be observed that not only the conversion rate of ethanol continuously increases, but also the selectivity of glycolic acid in liquid products gradually improves to as high as 95.1% with 8 h reaction time (Figure S21). Extending the reaction time from 1 to 8 h did not significantly change the carbon dioxide selectivity. This indicates that prolonging the reaction time is beneficial for reducing the generation of byproducts or intermediates. Additionally, it was observed that the catalytic activity was nearly zero (Figure 3e) without O_2 , indicating that oxygen is essential for the formation of glycolic acid. When the O₂ pressure was below 1.5 MPa, N₂ backfilling ensured a constant total pressure of 1.5 MPa. The catalytic activity was maximized at an O₂ partial pressure of 1.5 MPa. Increasing the O₂ partial pressure to 2 MPa caused a sharp increase of CO₂ selectivity to 42.4% (Table S9), indicating that excessive oxygen pressure promotes overoxidation of both the substrate and product to CO2. Furthermore, the stability of Rh₁/AC-SNI₄₀₀ catalyst was verified over 10 reaction cycles, showing ignorable activity decay under conditions of 150 °C, 1.5 MPa total pressure, and 1 h reaction time (Figure 3f).

Moreover, we performed controlled experiments varying water and ethanol quantities (Figures S22 and S23). Reducing water slightly enhanced the activity but significantly increased CO₂ selectivity (Table S10). Excess water dilutes the ethanol concentration, reducing the contact frequency among the

substrate, O₂, and catalyst, which in turn diminishes the reaction rate. Therefore, the appropriate amount of water, temperature, and O₂ partial pressure can prevent the overoxidation of the product. Increasing the ethanol amount improved reaction conversion while maintaining high selectivity toward glycolic acid. Across these experiments, the carbon balance of the system remained consistently between 94% and 106%. As shown in Figure S24, the hot filtration experiment shows that the liquid-phase product concentration did not increase after catalyst removal but decreased. This confirms that Rh did not leach into the solution to form a homogeneous catalyst. The decline in the product concentration is attributed to further oxidation into CO₂.

2.3. Factors for the Excellent Performance of Rh₁/AC-SNI₄₀₀. Given the good catalytic performance of Rh₁/AC-SNI₄₀₀ in the direct oxidation of ethanol to glycolic acid, the synergistic coordination effects of heteroatoms on the electronic reconfiguration and reactant adsorption capabilities were further investigated. Bader charge analysis is typically employed to compare the absolute electron count around different atoms, enabling a quantitative assessment of charge states. In contrast, differential charge density analysis reveals regions of electron accumulation and depletion, thereby providing insight into the directionality of electron transfer. A comparison of the differential charge density and Bader charge changes for active sites with varying coordination environments reveals that the cooperative coordination effect of S/N/I significantly influences the electronic distribution (Figure 4a—c and Table S11). Affected by S/N/I on the carrier simultaneously, the electron cloud depletion in Rh₁/AC-SNI₄₀₀ appears around the Rh atom, with a Bader charge of 14.38lel and an electronic valence state of +0.62 eV. In contrast, the electron cloud around Rh is more enriched in Rh₁/AC-NI₄₀₀ and Rh₁/AC-SI₄₀₀, with Bader charges of 14.46lel and 14.62lel and valence states of +0.54 eV and +0.38 eV, respectively. The synergistic coordination of S/N/I in Rh₁/AC-SNI₄₀₀ enhances electron delocalization, leading to substantial charge transfer around the Rh atom. This electronic configuration facilitates the interaction between the active site and ethanol by making the attack of the oxygen atom in ethanol on the Rh active site more effectively.

This conclusion was further supported by additional characterizations and DFT analyses. Ethanol temperatureprogrammed desorption (C₂H₅OH-TPD) was employed to investigate the ethanol adsorption properties. As shown in Figure 4d-e and Figures S25 and S26, the desorption temperature of ethanol decreased to 129 °C on Rh₁/AC-SNI₄₀₀, which is the lowest among Rh₁/AC-SNI₆₀₀, Rh₁/AC- SNI_{800} , $Rh_1/AC\text{-}SI_{400}$, and $Rh_1/AC\text{-}NI_{400}$. This result highlights that the synergistic coordination effect of S/N/I significantly reduces the desorption energy barrier of ethanol. DFT calculations were performed to evaluate the adsorption energy barrier of ethanol on single-Rh sites with different coordination environments. As illustrated in Figure 4f, the ethanol adsorption energy barrier is -0.53 eV over Rh₁/AC-SNI₄₀₀, which is significantly lower than that of Rh₁/AC-NI₄₀₀ (+0.08 eV) and Rh₁/AC-SI₄₀₀ (+0.25 eV), aligning well with the experimental results. Additionally, the Bader charge and differential charge density changes of various Rh active sites after ethanol adsorption were calculated. As shown in Figure S27 and Table S12, the synergistic effects of S/N/I coordination led to a more pronounced depletion of electrons (indicated in green) around the Rh atom. This results in a

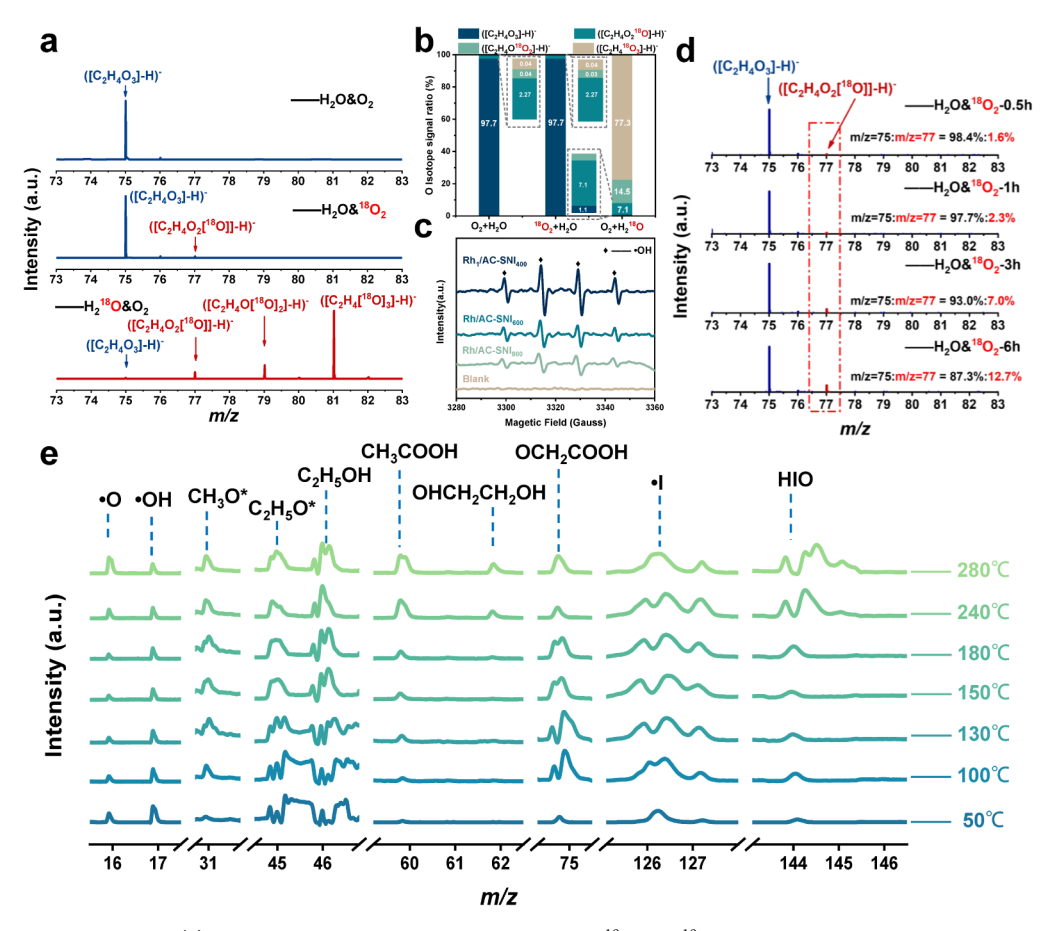


Figure 5. In situ experiments of (a) glycolic acid LC-MS results with $H_2O/^{18}O_2/H_2^{18}O$ isotope labeled on Rh_1/AC - SNI_{400} and (b) signal distribution of LC-MS results. (c) EPR spectra of the ethanol oxidation reaction over Rh_1/AC - SNI_{400} , Rh/AC- SNI_{600} , and Rh/AC- SNI_{800} . DMPO was added into the reaction mixture as the radical trapping agent. (d) $^{18}O_2$ labeling LC-MS results on Rh_1/AC - SNI_{400} with different reaction times. (e) In situ FEL-TOF/MS spectrometry on Rh_1/AC - SNI_{400} using $C_2H_5OH/CO/O_2/H_2O/I_2/Ar$ from 50 to 280 °C.

higher oxidized valence of Rh, with a Bader charge of 14.09lel. These findings suggest that the simultaneous coordination of S, N, and I facilitates more electron transfer from Rh, strengthening the Rh-O bond. Consequently, the formation of Rh-OCH2CH3 became more favorable. The simulated length of the O-H bond adsorbed on Rh₁/AC-SNI₄₀₀ is 0.99 Å, longer than those adsorbed on Rh₁/AC-NI₄₀₀ (0.98 Å) and Rh₁/AC-SI₄₀₀ (0.97 Å), further supporting the conclusions (Table S12). Additionally, the energy barriers for the β -C-H activation of ethanol over the three catalysts are illustrated in Figure 4l. The results revealed that Rh₁/AC-SNI₄₀₀ requires only +0.79 eV, which is significantly lower than those on Rh₁/ $AC-NI_{400}$ (+0.95 eV) and $Rh_1/AC-SI_{400}$ (+1.36 eV). These experimental and theoretical findings demonstrate that the synergistic S/N/I coordination effect optimizes the electronic properties of the single-Rh site, enhancing its ability to adsorb and activate substrates effectively.

In situ diffuse reflectance infrared Fourier transform spectroscopy (in situ DRIFTS) experiments were conducted to investigate the intermediates of the ethanol direct oxidation reaction on Rh₁/AC-SNI₄₀₀. As shown in Figure 4g and h, the signals appearing at 3506 cm⁻¹ and 1639 cm⁻¹ belonged to O–H stretching of water, while the signals of ethanol were detected at 3218 cm⁻¹ and 1259 cm⁻¹ (O–H stretching), 2976 cm⁻¹ and 1393 cm⁻¹ (*CH₃), 2898 cm⁻¹ and 1443 cm⁻¹ (*CH₂), and 873 cm⁻¹ (C–O stretching). Additionally, the C=O stretch corresponding to the acetyl group of acetic

acid appeared at 1747 cm⁻¹ as the reaction progressed. The relatively weak intensity of this peak reflects the low selectivity for the acetic acid product. In the absence of I2, the reaction products comprise only acetaldehyde and acetic acid (Figure 3a). Consequently, the in situ DRIFTS spectrum in Figure 4k exhibits only the acetyl peak at 1747 cm⁻¹, with no signal at 1612 cm⁻¹. However, a distinct peak emerges at 1612 cm⁻¹ when I₂ is included. This observation confirms that the 1612 cm⁻¹ peak is not attributable to the C=O bonds of acetaldehyde or acetic acid, but rather corresponds to the 2hydroxyacetyl species, which acts as a key intermediate in the formation of glycolic acid. 50 Furthermore, the Rh–OH peak was detected at 3665 cm⁻¹, showing the bound between hydroxyl groups and the single-Rh sites. \$1,52 After purging with nitrogen, the signals of ethyl species adsorbed on the single-Rh site remained, with the disappearance of most peaks (Figure \$28). Furthermore, a weak peak emerged at 1583 cm⁻¹, which can be attributed to the carboxyl group of glycolic acid. 50,53 In contrast, only the acetyl group signal was observed in the controlled experiment without the addition of I₂, with no detection of characteristic peaks for 2-hydroxyacetyl species or glycolic acid during the in situ reaction process (Figure 4j-k, and Figure S28). It was observed that the addition of I2 promotes the generation of •OH species from H2O by comparing the •OH peak intensity of water. DFT calculations revealed that iodine radicals activate H₂O molecules over Rh₁/ AC-SNI₄₀₀ to form HIO intermediates and ●OH species with

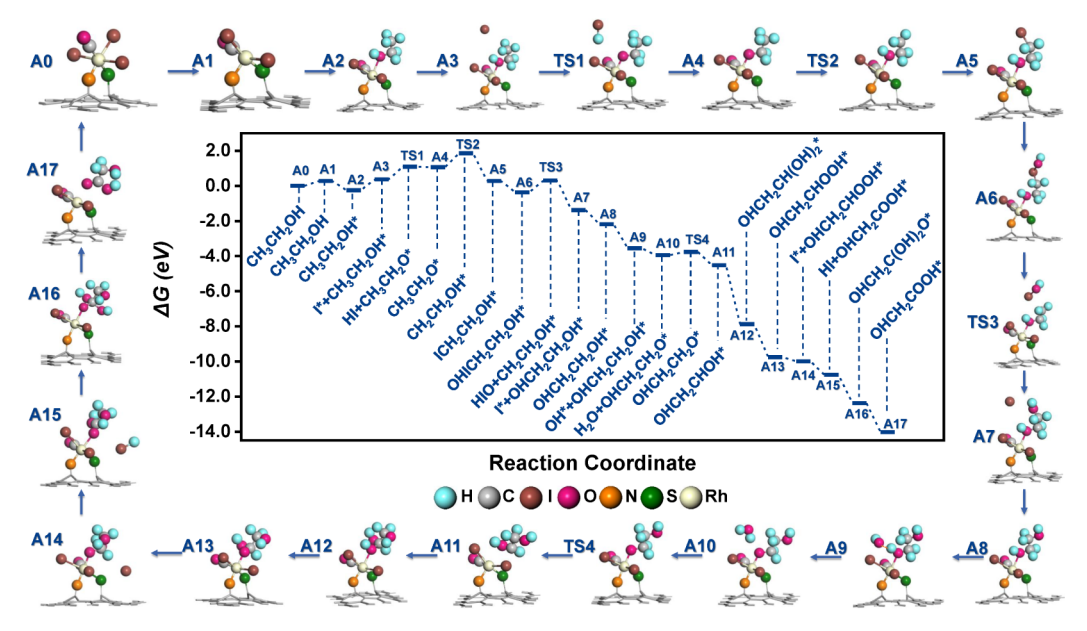


Figure 6. DFT calculations. The reaction pathway of ethanol oxidation to glycolic acid on the Rh_1/AC - SNI_{400} catalyst, involving O_2 , I_2 , and ethanol, includes the structures of key intermediates and their corresponding Gibbs free energy (ΔG) changes. States 1–17 represent different elementary steps in the reaction pathway, while TS denotes the transition states. The color scheme used is as follows: cyan spheres for H; gray spheres for C; red spheres for O; green spheres for S; yellow spheres for N; brown spheres for I; and beige spheres for Rh.

an energy barrier of +0.25 eV. In contrast, the activation of $\rm H_2O$ to generate $\bullet \rm OH$ solely via $\rm Rh_1/AC\text{-}SNI_{400}$ requires an energy barrier of +0.58 eV. The addition of $\rm I_2$ significantly reduces the activation energy of $\bullet \rm OH$ generation from $\rm H_2O$ (Figure 4i and Figure S29). These findings confirm the formation pathway of glycolic acid and highlight the critical role of $\rm I_2$ in the reaction.

Isotope labeling experiments are effective techniques to trace element changes in reactants and products. The oxygen transfer process during the conversion of ethanol to glycolic acid on Rh₁/AC-SNI₄₀₀ was investigated using liquid chromatography-mass spectrometry (LC-MS), as shown in Figure 5a and Table S13. Initially, experiments with common H₂O and O₂ revealed a signal corresponding to glycolic acid ([C₂H₄O₃]-H)⁻, confirming that LC-MS can effectively detect the reaction products. When ¹⁸O₂ was used to replace the O_2 , only a very small amount of $([C_2H_4O_2[^{18}O]]-H)^$ was detected, indicating that most of the oxygen in glycolic acid originates from other reactants. By replacing H2O with H₂¹⁸O, the resulting signals, from strongest to weakest, were detected as $([C_2H_4[^{18}O]_3]-H)^- > ([C_2H_4O[^{18}O]_2]-H)^- > ([C_2H_4O_2[^{18}O]]-H)^-$ in Figure 5b. These results suggest that H₂O directly participates in the reaction, and the -OH group in ethanol exchanges with •OH from water, forming $([C_2H_4[^{18}O]_3]-H)^-$. All of the oxygen atoms of glycolic acid come from water via the catalytic action of single-Rh sites. Control experiments demonstrated that the reaction scarcely proceeds without O₂ (Figure 3e), indicating that O₂ is crucial for generating •OH from H₂O. An isotope labeling experiment was designed to verify the oxygen exchange processes, including addressing the involvement of H_2O and the transfer of oxygen from O2 to H2O. Using 5,5-dimethyl-1-pyrroline Noxide (DMPO) as a radical scavenger, electron paramagnetic resonance (EPR) spectroscopy was conducted. 54,55 As shown in Figure 5c, •OH radicals dissociated from H2O were captured by DMPO in the liquid phase, producing clear signals which directly indicate their involvement in the oxidation of

ethanol to glycolic acid over the ${
m Rh_1/AC\text{-}SNI_{400}}$ catalyst, while the blank experiment did not show any radical signals.

The distribution of ¹⁸O isotopes in H₂O after the reaction was investigated using gas chromatography-mass spectrometry (GC-MS). As shown in Figure S30, a minor m/z = 20signal was observed in the control experiment with normal O_2 , corresponding to the natural abundance of ¹⁸O in water. In contrast, the signal increased dramatically when ¹⁸O₂ was employed in the reaction, confirming that oxygen from O2 was transferred to H₂O after the reaction. Isotopic tracing experiments further revealed a novel oxygen shuttle mechanism mediated by water molecules, in which the •OH generated from the dissociation of water can insert into α and β -C-I formed from ethanol with the help of the O_2/I_2 triggering and replace the hydroxyl group of ethanol. Simultaneously, O₂ can combine with H species to form new H₂O molecules, thereby establishing a dynamic cycle of oxygen and water. To further validate this conclusion, we conducted a series of experiments with different reaction times using ¹⁸O₂. isotope exchange. As illustrated in Figure 5d, the relative abundance of the ([C₂H₄O₂[¹⁸O]]-H)⁻ species gradually increases from 1.69% to 12.7% over reaction times of 0.5, 1, 3, and 6 h, respectively. With the prolonged reaction time, ¹⁸O₂ was gradually converted into H₂¹⁸O water molecules, leading to the content enhancement of the $([C_2H_4O_2[^{18}O]]-H)^-$. This observation provides powerful evidence for the proposed reaction mechanism of oxygen shuttle in the system.

In situ free electron laser time-of-flight mass spectrometry (FEL-TOF/MS) was conducted using a vacuum ultraviolet free electron laser (VUV FEL) at the Dalian Coherent Light Source (Figure S31). S6,57 As shown in Figure Se, when $C_2H_5OH/O_2/H_2O/Ar$ passed through the mixture of I_2 and Rh_1/AC -SNI₄₀₀, the signals of oxygen radicals O0 (M/z = 16), hydroxyl radicals O1 (M/z = 17), and iodine radicals O1 (M/z = 126.9) were captured with increasing temperature. This indicates the dissociation of O_2 , O2, and O3 active sites of the O4 the O5 catalyst. Due to the excess O6 the O9 has a condition of O9 and O9 to the excess O9 has a condition of the O9 has a condition of O9 has a

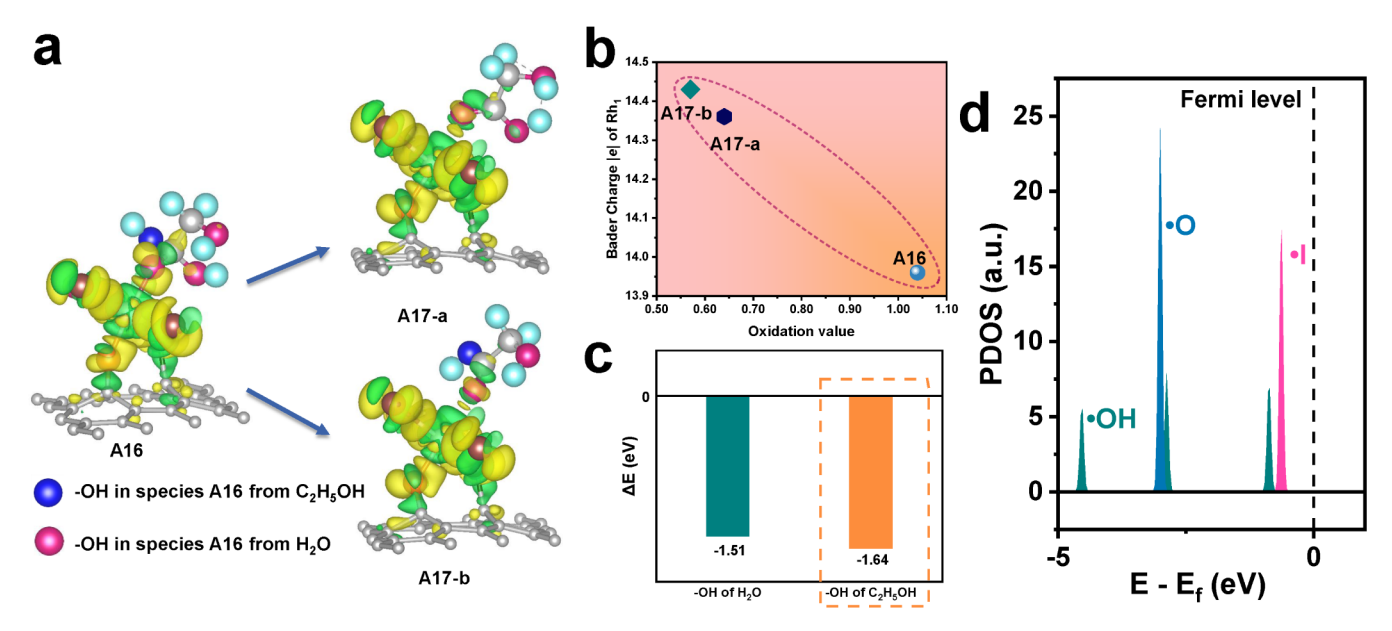


Figure 7. DFT calculations. (a) Depicts the difference in charge density changes of A16 species in Figure 6 after removing two OH groups in units of negative charge e—. In the difference charge density diagram, the green area indicates electron depletion, while the yellow area indicates electron accumulation. (b) Bader charge of A16 and A17 species in Figure 6 and the change of Rh valence. (c) Desorption energy diagram of two −OH groups on Rh active sites. (d) Projected state density of •O, •I, and •OH radicals.

system, the signals of $C_2H_5O^*$ (m/z = 45) and C_2H_5OH (m/z= 46) exhibited strong multiple peaks at lower temperatures. As the reaction system temperature enhanced, the peak intensity gradually decreased due to the conversion of ethanol into glycolic acid and other intermediates. The signal of acetic acid (m/z = 60) was observed as the temperature increased. However, the intensity of glycolic acid (m/z = 75) reached its maximum at 180 °C and then decreased, which could be attributed to the decomposition of glycolic acid under hightemperature conditions. Additionally, signals of ethylene glycol intermediate species (OHCH₂CH₂OH*) at m/z = 62 and hypoiodous acid species (HIO) at m/z = 143.9 were also observed, indicating possible intermediate species of ethylene glycol and HIO during the formation of glycolic acid. From the results presented above, it is evident that H₂O provides the O source for glycolic acid. O2 and I2 activate H2O to form hydroxyl radicals (•OH).

Density functional theory (DFT) calculations were employed to simulate the reaction pathways and associated energy changes (Figure 6 and Table S14), providing further insights into the mechanism of ethanol oxidation to glycolic acid over the Rh₁/AC-SNI₄₀₀ catalyst in the presence of I₂. DFT calculations revealed that the reformed Rh active site (A1) preferentially adsorbs the oxygen atom of ethanol to form a Rh-OHCH₂CH₃ structure (A2). Via the stimulation of the O2 under a specific temperature, I2 generates •I radicals. The energies required for \bullet I radicals to attack the β -C-H bond of ethanol and the Rh-OH bond were both calculated (Figure S32). It is shown that •I radicals more easily abstract hydrogen from Rh-OH, resulting in the transition state Rh-OCH₂CH₃ (TS1) and HI. After HI removal, Rh-OCH₂CH₃ undergoes intramolecular hydrogen transfer, yielding Rh-OHCH2CH2 species (TS2) with a rate-determining step energy barrier of 0.79 eV. In fact, the iodine radical plays a critical role in the formation of the TS2 intermediate. The energy barrier for breaking the β -C-H bond with the assistance of iodine radicals is 0.8 eV higher than that without them (Figure S33).

In the presence of •I and •OH radicals, Rh–OCH₂CH₂I (A5) and Rh-OCH₂CH₂IOH species (A6) form in succession. The desorption of HIO requires 0.67 eV of energy (TS3), and subsequent •OH radical attack easily generates Rh-OH-CH₂CH₂OH species (A8). Since glycol desorption requires 0.26 eV of energy, only trace amounts of glycol were detected in the VUV-FEL experiment (Figure 5e). Further attack of the •OH radical results in the formation of Rh-O(H₂O)-CH₂CH₂OH species (A10), which undergoes dehydration to produce a transient species TS4. Due to the instability of TS4, a brief intramolecular hydrogen transfer occurs, yielding Rh-OHCHCH2OH species (A11). Continuous •OH radical attack successively generates Rh-OH-CHOHCH2OH species (A12) and Rh-O-CHOHCH2OH species (A13). Notably, •OH radicals preferentially bond to Rh rather than to the oxygen atom of ethanol. The •I radicals more easily attack the α-C-H bond of Rh-O-CHOHCH2OH species (A14), forming Rh–O–COHCH₂OH species (A15). Further attack of the •OH radical results in the formation of multiple OH-competitive adsorption species, Rh-O-C(OH)₂CH₂OH (A16). However, this species is highly unstable, and after OH desorption, glycolic acid detaches from the Rh active site (A17), allowing the Rh site to re-enter the catalytic cycle. It is worth noting that the signal of 2-hydroxyacetyl (1612 cm⁻¹) from the secondary desorption of OH from Rh-O-C(OH)₂CH₂OH (A16) was captured in the in situ DRIFT experiment (Figure 4h and Figure S34).

As shown in Figure 7, differential charge density analysis was conducted to explore the possible –OH desorption process for the transformation of Rh–O–C(OH)₂CH₂OH (A16) to Rh–HOOCCH₂OH (A17) species during the reaction pathway in Figure 6. When the OH inherited from original ethanol (bold OH in Rh–O–OHC(OH)CH₂OH) was removed (A17a in Figure 7a), the Bader charge of Rh increased from 13.96 to 14.36 eV, and the Rh–O bond exhibited a length of 2.29 Å, with a valence state of +0.64 and an energy barrier of –1.64 eV (Figure 7b,c). In contrast, the removal of the OH from water

in A16 (bold OH in Rh-O-OHC(OH)CH₂OH, A17b in Figure 7a) resulted in an increase in the Bader charge of Rh from 13.96 to 14.43 eV, with an Rh-O bond length of 2.31 Å and an oxidized valence of +0.57 for Rh species (Figure 7b). The corresponding OH desorption energy in this case is -1.51eV, as shown in Figure 7c. This indicates that the OH group inherited from ethanol in the A16 species is more prone to desorption, leading to a more stable A17 structure. This also explains that the oxygen atoms in the glycolic acid product all originate from H₂O from the point of energy. Additionally, a simple simulation of the reaction pathway leading to acetaldehyde and acetic acid in the absence of I2 was performed, while the oxidant was either the O radical or OH radical, respectively (Figure S35 and S36 and Table S15). The energy barrier to extract a hydrogen atom from Rh-OH-CH₂CH₃ under only the action of •O radicals is +0.91 eV, higher than 0.79 eV with the assistance of •I radicals (Figure \$36). It only leads to the formation of acetaldehyde, which was subsequently oxidized to acetic acid. This suggests that the addition of I2 assists the single-Rh site to activate hydrogen. The high reactivity of the iodine radical (•I) is due to its significantly higher density of states (DOS) near the Fermi level compared with other species (Figure 7d). The hydroxyl radical (•OH), with a second DOS, also demonstrates strong insertion capability. The oxygen shuttle via water mediation can accelerate the conversion of ethanol to glycolic acid at the Rh active site.

3. CONCLUSION

In summary, we developed a sulfur/nitrogen/iodine (S/N/I) synergistically coordinated single-atom rhodium catalyst (Rh₁/ AC-SNI400) via a multiple-ligand induction strategy. This system enables the direct and efficient conversion of ethanol to glycolic acid under the O2/I2 activation, exhibiting the best performance at 160 °C with a TOF of ca. 250 h⁻¹ and glycolic acid selectivity in liquid products of 93%, outperforming Rh nanoparticles by 16-fold. The optimized S/N/I synergistical coordination enhances electron delocalization around Rh sites, substantially reducing the activation barriers of critical reaction steps. The identified key intermediate of activated iodine radicals (\bullet I) preferentially abstracts β -C-H hydrogen atoms from ethanol, thereby redirecting the reaction trajectory. A water-mediated oxygen shuttle mechanism unveils that hydroxyl radicals (•OH) generated via H2O dissociation insert into α -C and β -C to form the -OH group. The highly reactive •OH radicals will also replace the original OH of ethanol to form C=O. Meanwhile, O₂ reacts with the iodine radical and hydrogen species from ethanol and water to generate hypoiodous acid (HIO) as a key intermediate. Subsequently, HIO undergoes decomposition to regenerate H₂O and O₂, thereby completing the water-mediated oxygen shuttle catalytic cycle. This energy-efficient and highly selective reaction mechanism offers a sustainable pathway for ethanol conversion.

ASSOCIATED CONTENT

Supporting Information

The Supporting Information is available free of charge at https://pubs.acs.org/doi/10.1021/jacs.5c07150.

Experimental procedures; additional catalytic data; ¹H NMR spectra; additional characterization data; proposed mechanism (PDF)

AUTHOR INFORMATION

Corresponding Authors

Yunjie Ding — Dalian National Laboratory for Clean Energy, Dalian Institute of Chemical Physics, Chinese Academy of Sciences, Dalian 116023, China; State Key Laboratory of catalysis, Dalian Institute of Chemical Physics, Chinese Academy of Sciences, Dalian 116023, China; ◎ orcid.org/0000-0001-8894-9648; Email: dyj@dicp.ac.cn

Li Yan – Dalian National Laboratory for Clean Energy, Dalian Institute of Chemical Physics, Chinese Academy of Sciences, Dalian 116023, China; Email: yanli@dicp.ac.cn

Xiangen Song — Dalian National Laboratory for Clean Energy, Dalian Institute of Chemical Physics, Chinese Academy of Sciences, Dalian 116023, China; Email: xiangensong@dicp.ac.cn

Authors

Bin Li – Dalian National Laboratory for Clean Energy, Dalian Institute of Chemical Physics, Chinese Academy of Sciences, Dalian 116023, China

Jiali Mu – Dalian National Laboratory for Clean Energy, Dalian Institute of Chemical Physics, Chinese Academy of Sciences, Dalian 116023, China

Guifa Long – Dalian National Laboratory for Clean Energy, Dalian Institute of Chemical Physics, Chinese Academy of Sciences, Dalian 116023, China; Guangxi Key Laboratory of Chemistry and Engineering of Forest Products, School of Chemistry and Chemical Engineering, Guangxi Minzu University, Nanning 530008, China

Yang Zhao – Dalian National Laboratory for Clean Energy, Dalian Institute of Chemical Physics, Chinese Academy of Sciences, Dalian 116023, China

Ende Huang – Dalian National Laboratory for Clean Energy, Dalian Institute of Chemical Physics, Chinese Academy of Sciences, Dalian 116023, China; University of Chinese Academy of Sciences, Beijing 100049, China

Siyue Liu – Dalian National Laboratory for Clean Energy, Dalian Institute of Chemical Physics, Chinese Academy of Sciences, Dalian 116023, China; University of Chinese Academy of Sciences, Beijing 100049, China

Yao Wei – Shanghai Synchrotron Radiation Facility, Shanghai Advanced Research Institute, Chinese Academy of Sciences, Shanghai 200120, China

Fanfei Sun – Shanghai Synchrotron Radiation Facility, Shanghai Advanced Research Institute, Chinese Academy of Sciences, Shanghai 200120, China

Siquan Feng – Dalian National Laboratory for Clean Energy, Dalian Institute of Chemical Physics, Chinese Academy of Sciences, Dalian 116023, China; ◎ orcid.org/0000-0003-1367-164X

Qiao Yuan — Dalian National Laboratory for Clean Energy, Dalian Institute of Chemical Physics, Chinese Academy of Sciences, Dalian 116023, China; University of Chinese Academy of Sciences, Beijing 100049, China; Ocid.org/

Xingju Li – Dalian National Laboratory for Clean Energy, Dalian Institute of Chemical Physics, Chinese Academy of Sciences, Dalian 116023, China

Yutong Cai — Dalian National Laboratory for Clean Energy, Dalian Institute of Chemical Physics, Chinese Academy of Sciences, Dalian 116023, China; University of Chinese Academy of Sciences, Beijing 100049, China

- Yue Zhang Dalian National Laboratory for Clean Energy, Dalian Institute of Chemical Physics, Chinese Academy of Sciences, Dalian 116023, China; University of Chinese Academy of Sciences, Beijing 100049, China
- Wenrui Dong State Key Laboratory of Molecular Reaction Dynamics, Dalian Institute of Chemical Physics, Chinese Academy of Sciences, Dalian 116023, China; Hefei National Laboratory, Hefei 230088, China; orcid.org/0000-0002-3640-1821
- Weiqing Zhang State Key Laboratory of Molecular Reaction Dynamics, Dalian Institute of Chemical Physics, Chinese Academy of Sciences, Dalian 116023, China; orcid.org/ 0000-0001-6518-4152
- Xueming Yang State Key Laboratory of Molecular Reaction Dynamics, Dalian Institute of Chemical Physics, Chinese Academy of Sciences, Dalian 116023, China; Department of Chemistry, Southern University of Science and Technology, Shenzhen 518055, China; orcid.org/0000-0001-6684-9187
- Dehui Deng Dalian National Laboratory for Clean Energy, Dalian Institute of Chemical Physics, Chinese Academy of Sciences, Dalian 116023, China; ⊙ orcid.org/0000-0001-9702-0531

Complete contact information is available at: https://pubs.acs.org/10.1021/jacs.5c07150

Author Contributions

◆B.L., J.M., and G.L. contributed equally.

Notes

The authors declare no competing financial interest.

ACKNOWLEDGMENTS

The financial support for this work was provided by the National Key R&D Program of China (No. 2023YFA1506604), the National Natural Science Foundation of China (22372161), the China Postdoctoral Science Foundation (2025M770974), the Postdoctoral Fellowship Program (Grade B) of China Postdoctoral Science Foundation (GZB20250240) and the CAS Project for Young Scientists in Basic Research (YSBR-022). We also acknowledge the Shanghai Synchrotron Radiation Facility (SSRF) for providing beam time for the XAFS experiments. We thank the staff members of the Free Radical Detection Station (31127.02.DCLS.FRDS) at the Dalian Coherent Light Source (31127.02.DCLS) for their technical support and assistance in data collection and analysis.

REFERENCES

- (1) Zanchet, D.; Santos, J. B. O.; Damyanova, S.; Gallo, J. M. R.; Bueno, J. M. C. Toward understanding metal-catalyzed ethanol reforming. *ACS Catal.* **2015**, *5* (6), 3841–3863.
- (2) Meyer, C. C.; Stafford, N. P.; Cheng, M. J.; Krische, M. J. Ethanol: Unlocking an abundant renewable C_2 -feedstock for catalytic enantioselective C-C coupling. *Angew. Chem., Int. Ed.* **2021**, *60* (19), 10542–10546.
- (3) Cai, W.; Wang, F.; Zhan, E.; Vanveen, A.; Mirodatos, C.; Shen, W. Hydrogen production from ethanol over Ir/CeO₂ catalysts: A comparative study of steam reforming, partial oxidation and oxidative steam reforming. *J. Catal.* **2008**, 257 (1), 96–107.
- (4) Nozawa, T.; Mizukoshi, Y.; Yoshida, A.; Naito, S. Aqueous phase reforming of ethanol and acetic acid over TiO₂ supported Ru catalysts. *Appl. Catal., B* **2014**, *146*, 221–226.

- (5) Llorca, J. Effect of sodium addition on the performance of Co–ZnO-based catalysts for hydrogen production from bioethanol. *J. Catal.* **2004**, 222 (2), 470–480.
- (6) Huber, G. W.; Iborra, S.; Corma, A. Synthesis of transportation fuels from biomass: Chemistry, catalysts, and engineering. *Chem. Rev.* **2006**, *106* (9), 4044–4098.
- (7) de Souza, E. F.; Pacheco, H. P.; Miyake, N.; Davis, R. J.; Toniolo, F. S. Computational and experimental mechanistic insights into the ethanol-to-butanol upgrading reaction over MgO. *ACS Catal.* **2020**, *10* (24), 15162–15177.
- (8) Bedia, J.; Barrionuevo, R.; Rodríguez-Mirasol, J.; Cordero, T. Ethanol dehydration to ethylene on acid carbon catalysts. *Appl. Catal., B* **2011**, *103* (3–4), 302–310.
- (9) Sun, H.; Li, L.; Chen, Y.; Kim, H.; Xu, X.; Guan, D.; Hu, Z.; Zhang, L.; Shao, Z.; Jung, W. Boosting ethanol oxidation by NiOOH-CuO nano-heterostructure for energy-saving hydrogen production and biomass upgrading. *Appl. Catal., B* **2023**, 325, 122388.
- (10) Yunhai, S.; Houyong, S.; Deming, L.; Qinghua, L.; Dexing, C.; Yongchuan, Z. Separation of glycolic acid from glycolonitrile hydrolysate by reactive extraction with tri-n-octylamine. *Sep. Purif. Technol.* **2006**, 49 (1), 20–26.
- (11) Yunhai, S.; Houyong, S.; Haiyong, C.; Deming, L.; Qinghua, L. Synergistic extraction of glycolic acid from glycolonitrile hydrolysate. *Ind. Eng. Chem. Res.* **2011**, *50* (13), 8216–8224.
- (12) Yue, H.; Zhao, Y.; Ma, X.; Gong, J. Ethylene glycol: Properties, synthesis, and applications. *Chem. Soc. Rev.* **2012**, *41* (11), 4218–4244.
- (13) Zhu, Z.; Kang, G.; Sun, Y.; Yu, S.; Li, M.; Xu, J.; Cao, Y. An experimental study on synthesis of glycolic acid via carbonylation of formaldehyde using PTFE membrane contactor. *J. Membr. Sci.* **2019**, 586, 259–266.
- (14) Yang, S.-B.; Chien, I. L. Rigorous design and optimization of methyl glycolate production process through reactive distillation combined with a middle dividing-wall column. *Ind. Eng. Chem. Res.* **2019**, 58 (13), 5215–5227.
- (15) Witzemann, E. J. The preparation of glycollic acid. *J. Am. Chem. Soc.* **1917**, 39 (1), 109–112.
- (16) Yang, J.; Cheng, J.; Tao, J.; Higashi, M.; Yamauchi, M.; Nakashima, N. Wrapping multiwalled carbon nanotubes with anatase titanium oxide for the electrosynthesis of glycolic acid. *ACS Appl. Nano Mater.* **2019**, *2* (10), 6360–6367.
- (17) Wen, C.; Cui, Y.; Chen, X.; Zong, B.; Dai, W.-L. Reaction temperature controlled selective hydrogenation of dimethyl oxalate to methyl glycolate and ethylene glycol over copper-hydroxyapatite catalysts. *Appl. Catal.*, B **2015**, *162*, 483–493.
- (18) van Haasterecht, T.; van Deelen, T. W.; de Jong, K. P.; Bitter, J. H. Transformations of polyols to organic acids and hydrogen in aqueous alkaline media. *Catal. Sci. Technol.* **2014**, *4* (8), 2353–2366.
- (19) Qi, J.; Finzel, J.; Robatjazi, H.; Xu, M.; Hoffman, A. S.; Bare, S. R.; Pan, X.; Christopher, P. Selective methanol carbonylation to acetic acid on heterogeneous atomically dispersed ReO₄/SiO₂ catalysts. *J. Am. Chem. Soc.* **2020**, *142* (33), 14178–14189.
- (20) Zhang, L.; Yang, X.; Lin, J.; Li, X.; Liu, X.; Qiao, B.; Wang, A.; Zhang, T. On the coordination environment of single-atom catalysts. *Acc. Chem. Res.* **2025**, 58 (12), 1878–1892.
- (21) Xu, W.; Liu, H.-X.; Hu, Y.; Wang, Z.; Huang, Z.-Q.; Huang, C.; Lin, J.; Chang, C.-R.; Wang, A.; Wang, X.; et al. Metal-oxo electronic tuning via in situ CO decoration for promoting methane conversion to oxygenates over single-atom catalysts. *Angew. Chem., Int. Ed.* **2024**, 63 (16), No. e202315343.
- (22) Liu, L. C.; Corma, A. Metal catalysts for heterogeneous catalysis: From single atoms to nanoclusters and nanoparticles. *Chem. Rev.* 2018, *118* (10), 4981–5079.
- (23) Cui, X.; Li, W.; Ryabchuk, P.; Junge, K.; Beller, M. Bridging homogeneous and heterogeneous catalysis by heterogeneous singlemetal-site catalysts. *Nat. Catal.* **2018**, *1* (6), 385–397.
- (24) Sun, Z.; Shi, W.; Smith, L. R.; Dummer, N. F.; Qi, H.; Sun, Z.; Hutchings, G. J. Concerted catalysis of single atom and nanocluster

- enhances bio-ethanol activation and dehydrogenation. Nat. Commun. **2025**, 16 (1), 3935.
- (25) Yang, J.; Cui, Y.; Zhao, Y.; Purdy, S. C.; Zhang, J.; Liu, H.; Zheng, Y.; Nie, L.; Li, Z. Spatially aligned binary single-site catalyst on defective SiO₂ for cascading reactions. J. Am. Chem. Soc. 2025, 147 (25), 22084-22091.
- (26) Gerber, I. C.; Serp, P. A theory/experience description of support effects in carbon-supported catalysts. Chem. Rev. 2020, 120 (2), 1250-1349.
- (27) Yan, H.; Zhao, X.; Guo, N.; Lyu, Z.; Du, Y.; Xi, S.; Guo, R.; Chen, C.; Chen, Z.; Liu, W.; et al. Atomic engineering of high-density isolated Co atoms on graphene with proximal-atom controlled reaction selectivity. Nat. Commun. 2018, 9 (1), 3197.
- (28) Sá, J.; Goguet, A.; Taylor, S. F. R.; Tiruvalam, R.; Kiely, C. J.; Nachtegaal, M.; Hutchings, G. J.; Hardacre, C. Influence of methyl halide treatment on gold nanoparticles supported on activated carbon. Angew. Chem., Int. Ed. 2011, 50 (38), 8912-8916.
- (29) Zhou, Y.; Wei, F.; Qi, H.; Chai, Y.; Cao, L.; Lin, J.; Wan, Q.; Liu, X.; Xing, Y.; Lin, S.; Wang, A.; Wang, X.; Zhang, T. Peripheralnitrogen effects on the Ru1 centre for highly efficient propane dehydrogenation. Nat. Catal. 2022, 5 (12), 1145-1156.
- (30) Li, Z.; Chen, Y.; Ji, S.; Tang, Y.; Chen, W.; Li, A.; Zhao, J.; Xiong, Y.; Wu, Y.; Gong, Y.; Yao, T.; Liu, W.; Zheng, L.; Dong, J.; Wang, Y.; Zhuang, Z.; Xing, W.; He, C.-T.; Peng, C.; Cheong, W.-C.; Li, Q.; Zhang, M.; Chen, Z.; Fu, N.; Gao, X.; Zhu, W.; Wan, J.; Zhang, J.; Gu, L.; Wei, S.; Hu, P.; Luo, J.; Li, J.; Chen, C.; Peng, Q.; Duan, X.; Huang, Y.; Chen, X.-M.; Wang, D.; Li, Y. Iridium single-atom catalyst on nitrogen-doped carbon for formic acid oxidation synthesized using a general host-guest strategy. Nat. Chem. 2020, 12 (8), 764-772.
- (31) Panchakarla, L. S.; Subrahmanyam, K. S.; Saha, S. K.; Govindaraj, A.; Krishnamurthy, H. R.; Waghmare, U. V.; Rao, C. N. R. Synthesis, structure, and properties of boron- and nitrogendoped graphene. Adv. Mater. 2009, 21 (46), 4726-4730.
- (32) Feng, S.; Mu, J.; Lin, X.; Song, X.; Liu, S.; Shi, W.; Zhang, W.; Wu, G.; Jiayue, Y.; Dong, W.; Yang, X.; Li, J.; Jiang, Z.; Ding, Y. Sulfur-poisoning on Rh NP but sulfur-promotion on single-Rh₁-site for methanol carbonylation. Appl. Catal., B 2023, 325, 122318.
- (33) Li, B.; Song, X.; Feng, S.; Yuan, Q.; Jiang, M.; Yan, L.; Ding, Y. Direct conversion of methane to oxygenates on porous organic polymers supported Rh mononuclear complex catalyst under mild conditions. Appl. Catal., B 2021, 293, 120208.
- (34) Feng, S.; Song, X.; Liu, Y.; Lin, X.; Yan, L.; Liu, S.; Dong, W.; Yang, X.; Jiang, Z.; Ding, Y. In situ formation of mononuclear complexes by reaction-induced atomic dispersion of supported noble metal nanoparticles. Nat. Commun. 2019, 10 (1), 5281.
- (35) Sun, J.; Jena, H. S.; Abednatanzi, S.; Liu, Y.-Y.; Leus, K.; Van Der Voort, P. A green alternative for the direct aerobic iodination of arenes using molecular iodine and a POM@MOF catalyst. ACS Appl. Mater. Interfaces 2022, 14 (33), 37681-37688.
- (36) Xin, H.; Hu, L.; Yu, J.; Sun, W.; An, Z. A green catalytic method for selective synthesis of iodophenols via aerobic oxyiodination under organic solvent-free conditions. Catal. Commun. **2017**, 93, 1-4.
- (37) Maity, A.; Frey, B. L.; Powers, D. C. Iodanyl radical catalysis. Acc. Chem. Res. 2023, 56 (14), 2026-2036.
- (38) Li, B.; Mu, J.; Long, G.; Song, X.; Huang, E.; Liu, S.; Wei, Y.; Sun, F.; Feng, S.; Yuan, Q.; et al. Water-participated mild oxidation of ethane to acetaldehyde. Nat. Commun. 2024, 15 (1), 2555.
- (39) Ryaboshapka, D.; Piccolo, L.; Aouine, M.; Bargiela, P.; Briois, V.; Afanasiev, P. Ultradispersed (Co)Mo catalysts with high hydrodesulfurization activity. Appl. Catal., B 2022, 302, 120831.
- (40) Wu, D.; Baaziz, W.; Gu, B.; Marinova, M.; Hernández, W. Y.; Zhou, W.; Vovk, E. I.; Ersen, O.; Safonova, O. V.; Addad, A.; Nuns, N.; Khodakov, A. Y.; Ordomsky, V. V. Surface molecular imprinting over supported metal catalysts for size-dependent selective hydrogenation reactions. Nat. Catal. 2021, 4 (7), 595-606.
- (41) Zhang, J.; Zhang, M.; Zeng, Y.; Chen, J.; Qiu, L.; Zhou, H.; Sun, C.; Yu, Y.; Zhu, C.; Zhu, Z. Single Fe atom on hierarchically porous S, N-codoped nanocarbon derived from porphyra enable

- boosted oxygen catalysis for rechargeable Zn-Air batteries. Small **2019**, 15 (24), 1900307.
- (42) Yang, H. B.; Hung, S.-F.; Liu, S.; Yuan, K.; Miao, S.; Zhang, L.; Huang, X.; Wang, H.-Y.; Cai, W.; Chen, R.; Gao, I.; Yang, X.; Chen, W.; Huang, Y.; Chen, H. M.; Li, C. M.; Zhang, T.; Liu, B. Atomically dispersed Ni(i) as the active site for electrochemical CO2 reduction. Nat. Energy 2018, 3 (2), 140-147.
- (43) Ge, X.; Di, H.; Wang, P.; Miao, X.; Zhang, P.; Wang, H.; Ma, J.; Yin, L. Metal-Organic Framework-Derived Nitrogen-Doped Cobalt Nanocluster Inlaid Porous Carbon as high-efficiency catalyst for advanced potassium-sulfur batteries. ACS Nano 2020, 14 (11), 16022-16035.
- (44) Fei, H.; Dong, J.; Feng, Y.; Allen, C. S.; Wan, C.; Volosskiy, B.; Li, M.; Zhao, Z.; Wang, Y.; Sun, H.; An, P.; Chen, W.; Guo, Z.; Lee, C.; Chen, D.; Shakir, I.; Liu, M.; Hu, T.; Li, Y.; Kirkland, A. I.; Duan, X.; Huang, Y. General synthesis and definitive structural identification of MN₄C₄ single-atom catalysts with tunable electrocatalytic activities. Nat. Catal. 2018, 1 (1), 63-72.
- (45) Gao, J. J.; Yang, H. B.; Huang, X.; Hung, S. F.; Cai, W. Z.; Jia, C. M.; Miao, S.; Chen, H. M.; Yang, X. F.; Huang, Y. Q.; Zhang, T.; Liu, B. Enabling direct H₂O₂ production in acidic media through rational design of transition metal single atom catalyst. Chem 2020, 6 (3), 658-674.
- (46) Wang, X.; Chen, Z.; Zhao, X.; Yao, T.; Chen, W.; You, R.; Zhao, C.; Wu, G.; Wang, J.; Huang, W.; Yang, J.; Hong, X.; Wei, S.; Wu, Y.; Li, Y. Regulation of coordination number over single Co sites: Triggering the efficient electroreduction of CO₂. Angew. Chem., Int. Ed. 2018, 57 (7), 1944-1948.
- (47) Gong, Y.-N.; Cao, C.-Y.; Shi, W.-J.; Zhang, J.-H.; Deng, J.-H.; Lu, T.-B.; Zhong, D.-C. Modulating the electronic structures of dualatom catalysts via coordination environment engineering for boosting CO₂ electroreduction. Angew. Chem. Int. Ed. 2022, 61 (51), No. e202215187.
- (48) Guzman, F.; Chuang, S. S. C. Tracing the reaction steps involving oxygen and IR observable species in ethanol photocatalytic oxidation on TiO₂. J. Am. Chem. Soc. 2010, 132 (5), 1502-1503.
- (49) Yang, W.; Zhao, H.; Song, H.; Yang, J.; Zhao, J.; Yan, L.; Chou, L. Vapor-phase ethanol carbonylation over Ni supported on activated carbon: Influence of the textural properties and oxygen-containing groups. Chem. Eng. J. 2023, 476, 146595.
- (50) Wang, H.; Jiang, B.; Zhao, T.-T.; Jiang, K.; Yang, Y.-Y.; Zhang, J.; Xie, Z.; Cai, W.-B. Electrocatalysis of ethylene glycol oxidation on bare and Bi-modified Pd concave nanocubes in alkaline solution: An interfacial infrared spectroscopic investigation. ACS Catal. 2017, 7 (3), 2033-2041.
- (51) Mao, Q.; Deng, K.; Yu, H.; Xu, Y.; Wang, Z.; Li, X.; Wang, L.; Wang, H. In situ reconstruction of partially hydroxylated porous Rh metallene for ethylene glycol-assisted seawater splitting. Adv. Funct. Mater. 2022, 32 (31), 2201081.
- (52) Zeng, L.; Chen, Y.; Sun, M.; Huang, Q.; Sun, K.; Ma, J.; Li, J.; Tan, H.; Li, M.; Pan, Y.; Liu, Y.; Luo, M.; Huang, B.; Guo, S. Cooperative Rh-O₅/Ni(Fe) site for efficient biomass upgrading coupled with H₂ production. J. Am. Chem. Soc. 2023, 145 (32), 17577-17587.
- (53) Wang, L.; Meng, H.; Shen, P. K.; Bianchini, C.; Vizza, F.; Wei, Z. In situ FTIR spectroelectrochemical study on the mechanism of ethylene glycol electrocatalytic oxidation at a Pd electrode. Phys. Chem. Chem. Phys. 2011, 13 (7), 2667-2673.
- (54) Song, H.; Meng, X.; Wang, S.; Zhou, W.; Wang, X.; Kako, T.; Ye, J. Direct and selective photocatalytic oxidation of CH₄ to oxygenates with O2 on cocatalysts/ZnO at room temperature in water. J. Am. Chem. Soc. 2019, 141 (51), 20507-20515.
- (55) Song, H.; Meng, X.; Wang, S.; Zhou, W.; Song, S.; Kako, T.; Ye, J. Selective photo-oxidation of methane to methanol with oxygen over dual-cocatalyst-modified titanium dioxide. ACS Catal. 2020, 10, 14318-14326.
- (56) Liu, C.; Qian, B.; Xiao, T.; Lv, C.; Luo, J.; Bao, J.; Pan, Y. Illustrating the fate of methyl radical in photocatalytic methane oxidation over Ag-ZnO by in situ synchrotron radiation photo-

ionization mass spectrometry. Angew. Chem., Int. Ed. 2023, 62 (32), No. e202304352.

(57) Chang, Y.; An, F.; Chen, Z.; Luo, Z.; Zhao, Y.; Hu, X.; Yang, J.; Zhang, W.; Wu, G.; Xie, D.; et al. Vibrationally excited molecular hydrogen production from the water photochemistry. *Nat. Commun.* **2021**, *12* (1), 6303.

